JMEPEG (2015) 24:2586–2596
DOI: 10.1007/s11665-015-1537-7

1059-9495/$19.00

Analysis of the Deformation and Damage Mechanisms of Pearlitic Steel by EBSD and "in-situ" SEM Tensile Tests

Habib Sidhom, H. Yahyaoui, C. Braham, and G. Gonzalez

(Submitted October 12, 2014; in revised form April 8, 2015; published online May 8, 2015)

The processes governing the deformation and damage of C70 pearlitic steel were investigated in nanometer and micrometer scales using electron backscatter diffraction technique and "in-situ" scanning electron microscope tensile testing. The ferrite behavior was identified by "in-situ" x-ray tensile tests. Investigations were carried out on annealed microstructure with two interlamellar spacings of Sp = 170 and Sp = 230 nm. It is shown that pearlite yielding is controlled by the deformation mechanisms occurring in ferrite. Deformation and damage mechanisms were proposed. At low strain, pearlite deforms homogeneously with low misorientation (< 5°) inside the pearlite colonies and elongates the cementite plates. At high strain, pearlite deforms heterogeneously in intense localized shear bands inside the more favorably oriented pearlite colonies. Misorientation reaches values up to 15°. Cementite deforms by an offset of lamella along the shear bands. The nucleation of these shear bands occurs at strain level of E_{11} = 7% for coarse pearlite and at a higher value for fine pearlite. Damage occurs by brittle fracture of the elongated cementite lamellae parallel to the tensile axis and which are developed by shear micro-cracks along the slip bands. The plastic-induced damage is thus delayed by the fine pearlite structure.

Keywords damage, deformation, EBSD, pearlitic steel, SEM, shear cracking, x-ray diffraction

1. Introduction

Pearlitic steels have important applications where high strength and wear resistance are required. They are usually used in the manufacturing of railroad rails, wire, and suspension cables (Ref 1-4). Nevertheless, various microstructural variables complicate the control of the pearlitic structure significantly in order to satisfy various use conditions which are sometimes contradictory. It was shown that pearlitic steel behavior is strongly dependent on microstructure characteristics like early austenitic grain size, pearlite colonies, volume fraction, and shape of cementite (Ref 5-9). Hyzak et al. (Ref 10) showed that pearlitic steel strength is primarily dependent on the interlamellar spacing (Sp), while the toughness is mainly influenced by the prior-austenite grain size. The interlamellar spacing also influences the pearlite yield strength (Ref 11), the work hardening, and the fracture stress significantly. Accordingly, modified Hall-Petch type relationship integrating the interlamellar spacing effect was developed by previous investigators (Ref 12, 13). The effect of this parameter is often explained by its role in the deformation mode and in the damage nucleation and growth under imposed loading trajectory. However, the provided explanations were controversial mainly when the distribution of strain and damage and their consequences on the pearlite behavior were concerned. Porter et al. (Ref 14) investigated the deformation modes operating in fine (Sp = 90 nm) and coarse pearlite (Sp = 400 nm) by an "in-situ" high-resolution scanning electron microscope (SEM). They reported significant differences in the deformation and in the fracture mechanisms between fine and coarse pearlites. They stated that fine pearlite deforms by homogeneous slip in both the cementite and the ferrite, while the coarse pearlite deforms by coarse slip in the ferrite and by homogeneous slip in the cementite. Dollar et al. (Ref 13) studied, by combining tensile tests and TEM examinations, the influence of deformation substructure on flow and fracture for a range of pearlites

Nomenclature

CLM	Circular line method ·
E_{11}	Macroscopic strain ·
EBSD	Electron backscatter diffraction technique ·
HT	Heat treatment ·
IPF	Inverse pole figure ·
GAM	Grain average misorientation ·
KAM	Kernel average images ·
PQM	Pattern quality map ·
Sp	Interlamellar spacing (nm) ·
SEM	Scanning electron microscope ·
σ_y	Yield stress ·
Σ_{11}	Macroscopic stress

Habib Sidhom, Mechanical, Materials and Processes Laboratory (LR99ES05), ENSIT, University of Tunis, 5, Avenue Taha Hussein, 1008, Tunis, Tunisia; **H. Yahyaoui**, Mechanical, Materials and Processes Laboratory (LR99ES05), ENSIT, University of Tunis, 5, Avenue Taha Hussein, 1008, Tunis, Tunisia and Laboratoire Procédés et Ingénierie en Mécanique et Matériaux (PIMM, CNRS UMR 8006), Arts et Métiers-ParisTech, 151 Bd de l'Hôpital, 75013, Paris, France; **C. Braham**, Laboratoire Procédés et Ingénierie en Mécanique et Matériaux (PIMM, CNRS UMR 8006), Arts et Métiers-ParisTech, 151 Bd de Hôpital, 75013, Paris, France; and **G. Gonzalez**, Laboratoire Procédés et Ingénierie en Mécanique et Matériaux (PIMM, CNRS UMR 8006), Arts et Métiers-ParisTech, 151 Bd de l'Hôpital, 75013, Paris, France and Instituto de Investigaciones en Materiales, Universidad Nacional Autónoma de México, Circuito Exterior S/N, Cd. Universitaria, A.P. 70-360, C.P. 04510, Coyoacán, Mexico. Contact e-mails: habib.sidhom@gmail.com, habib.sidhom@esstt.rnu.tn, Yahyaoui_houda08@yahoo.fr, chedly.braham@Ensam.eu, and joseggr.iim@gmail.com.

Table 1 Chemical composition of C70 pearlitic steel (wt.%)

C	Si	Mn	S	P	Ni	Cr	Mo	Cu	Al	Fe
0.68	0.192	0.846	0.010	0.010	0.114	0.160	0.027	0.205	0.042	Balance

from very coarse (Sp = 530 nm) to relatively fine (Sp = 130 nm) interlamellar spacings. They found that the yielding and the work hardening of pearlite are controlled by the deformation mechanisms occurring in the ferrite while the tensile fracture is determined by the fracture of cementite lamellae in the colonies with lamellae parallel to the tensile axis. Li et al. (Ref 15) identified the fracture mechanisms in the fully lamellar microstructure of AISI 1080 steel by ''in-situ'' TEM tensile tests. They showed that the damage mode in the lamellar pearlite consists of four stages: (a) the dislocation pile-ups in the ferrite-cementite interface; (b) the single crack nucleation; (c) the distribution of crack nucleation; and (d) the crack growth followed by final fracture. However, Yongbo (Ref 16) observed, in the case of 0.79% C pearlitic steel, by ''in-situ'' SEM examination, the occurrence of shear bands along the direction of the maximum shear stress regardless of the lamellar orientation. Furthermore, he showed that nucleation and propagation of micro-cracks occur along the shear deformation bands.

In summary, the mechanisms of deformation and fracture of the relatively ductile pearlitic steel is not fully clearly understood. In addition, the role of the interlamellar spacing has not received sufficient attention. Moreover, the effect of the nucleation and the growth of plastic-induced damage on the modification of the stress partitioning between the ferrite and the cementite is still unknown. This study aims at understanding the deformation mechanisms and the damage modes occurring in C70 pearlitic steel with interlamellar spacings of 230 and 170 nm, respectively by combining electron backscatter diffraction technique (EBSD) technique and ''in-situ'' SEM tensile tests. The behavior of ferrite is determined by ''in-situ'' x-ray tensile tests. The effect of the deformation and the damage distributions on the ferrite yielding and the stress partitioning between the ferrite and the cementite will be investigated by comparing the ''in-situ'' x-ray and ''in-situ'' SEM tensile tests results. The effect of interlamellar spacing on the strain level producing damage nucleation will be assessed and discussed.

2. Material and Annealed Microstructure

2.1 Material

The pearlitic steel EN C70 (SAE 1070), the subject of this study, is provided by ASCOMETAL-France in the form of 80 mm diameter cylindrical bars obtained by hot rolling. The chemical composition of this steel is given in Table 1.

Two annealing treatments have been selected to provide two pearlitic microstructural configurations with similar ductility of approximately 15% tensile elongation :

- HT1: Austenitizing at 1073 K for 0.5 H followed by air cooling;
- HT2: Austenitizing at 1323 K for 0.1 H followed by cooling under forced air;

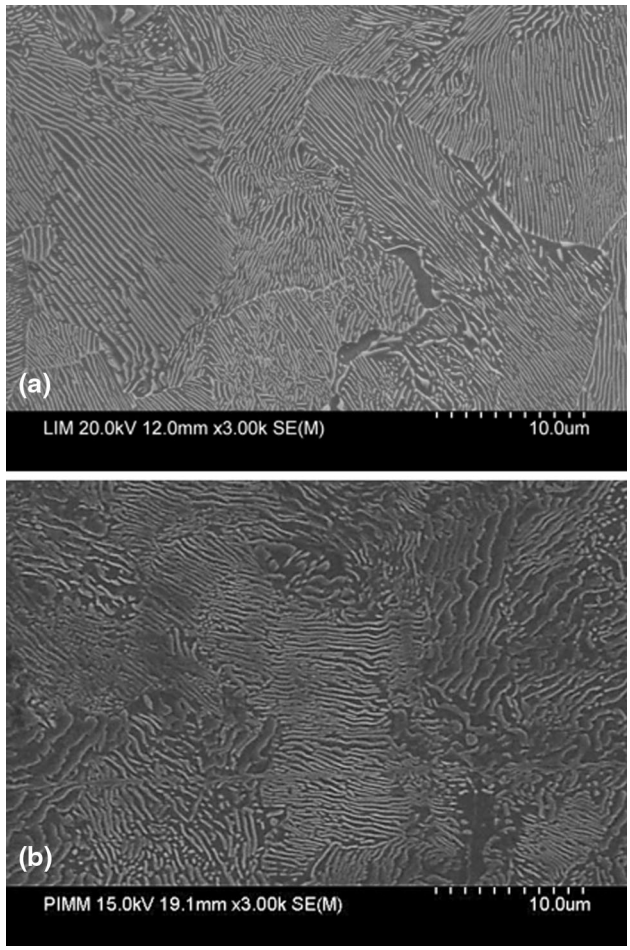

Fig. 1 Microstructures of C70 pearlitic steel: (a) austenitizing at 1073 K for 0.5 h followed by cooling under air (HT1); (b) austenitizing at 1323 K for 0.11 h followed by cooling under forced air (HT2)

2.2 Annealed Microstructure Characteristics

The random intercept method was used to determine the microstructure characteristics from SEM examinations. Samples were polished successively using fine silicon carbide papers from 100 to 4000 grit, then, finely polished with 3 μm water-based diamond suspension and finally, etched in 3% Nital solution during 10 s (Fig. 1). A circular line method (Ref 17) was used to determine the average interlamellar spacing (Fig. 2). Therefore, Sp was calculated using Eq 1:

$$S_p = \frac{0.5L}{N}, \quad \text{(Eq 1)}$$

where L is the circle perimeter and N is the number of intersections between the circular line and the cementite lamellae.

The analysis integrates the treatment of 25 micrographs in order to determine with more accuracy the average of the

interlamellar spacing. The microstructure characteristics and the mechanical properties of the two microstructures are summarized in Table 2. The structures of both pearlites differ mainly by the interlamellar spacings: Sp = 70 nm for what is called fine pearlite and Sp = 230 nm for the so-called coarse pearlite.

3. Experimental Setup

3.1 Specimen Geometries

Tensile specimens with a thickness of 2.1 mm and a length of 23 mm were used for "in-situ" x-ray tensile tests (Fig. 3). The "in-situ" SEM tensile tests were performed on specified specimen geometry as shown in Fig. 4.

3.2 "In-situ" X-ray Tensile Tests

The ferrite behavior was determined by x-ray "in-situ" tensile tests using a SET-X-type diffractometer under conditions listed in Table 3. The macroscopic force corresponding to the imposed displacement was monitored by an annular force sensor mounted on the test device (Fig. 3).The macroscopic strain was measured by strain gage adhering on the surface of the electropolished tensile samples. The $\sin^2\psi$ x-ray diffraction method was used to determine the ferrite stress (Ref 18).

3.3 EBSD Examinations

EBSD examinations were performed on polished and etched samples before and after tensile loading. This technique was used to evaluate the pearlite colonies orientations and the plastic-induced misorientations inside the pearlite colonies.

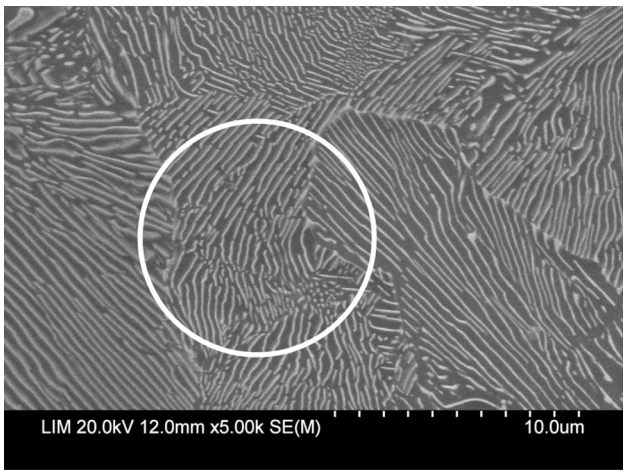

Fig. 2 Explored zone used for interlamellar spacing measuring

The *e-Flash™ HR EBSD* detector mounted on a JEOL 7600F SEM was used for electron image capture and the BRUKER ESPRIT software was used for EBSD data processing. EBSD maps and electron images for highly and slightly deformed regions were compared. The acquisition allows a high-quality EBSD results (~5% zero solutions at a speed of ~138 frames/s). The determination of the pearlite colony boundaries by EBSD was based on two criteria: (a) the misorientation angle threshold (equal to 5°), and (b) the minimum number of pixels (equal to 5).

Several post-processing algorithms were used for the EBSD treatment:

- The inverse pole figure (IPF) maps provide the relationship between the tensile axis and the crystallographic coordinate system.
- Pattern quality map (PQM) quantifies the microstructural details such as grain boundaries and deformation bands.
- The Schmid maps display the Schmid factor value (0-0.5) at each point of the map using gray levels; the brighter zones correspond to the higher Schmid factor (0.5).
- The grain average misorientation (GAM) provides information concerning the orientation changes inside grains.
- The kernel average images (KAM) were used to determine the local misorientation changes around a reference point (Kernel Center). This technique is very sensitive to local orientation changes.

3.4 "In-situ" SEM Tensile Tests

The evolution of deformation substructure and damage under tensile loading was followed by "in-situ" tensile tests performed with the specific device incorporated in Jeol JSM 6100 SEM. The tensile loading was carried out on specific polished and etched plate samples (Fig. 4). The macroscopic force corresponding to the imposed displacement was monitored by an annular force sensor mounted on the tensile test device.

4. Results

4.1 Effect of Interlamellar Spacing on Ferrite Stress

The "in-situ" x-ray tensile tests provide the ferrite stress-total true strain curves which reveal the effect of interlamellar spacing on the ferrite behavior (Fig. 5):

- The ferrite yield stress in the fine pearlitic structure (Sp = 170 nm) is equal to 280 MPa, which is higher than that of the coarse pearlitic structure (Sp = 230 nm) which is equal to 210 MPa.

Table 2 Heat treatments, metallurgical characteristics, and mechanical properties of the two microstructures

Annealing treatment	Colony size, µm	Grain size, µm	Interlamellar spacing sp, nm	Yield stress, MPa	Ultimate tensile strength, MPa	Elongation, %	Hardness HV_{50}
HT1: austenitizing at 1073 K for 0.5 h followed by air cooling	7.4	19	230	396	875	17	220 ± 10
HT2: austenitizing at 1323 K for 0.11 h followed by forced air cooling	7.9	26	170	498	997	15	270 ± 15

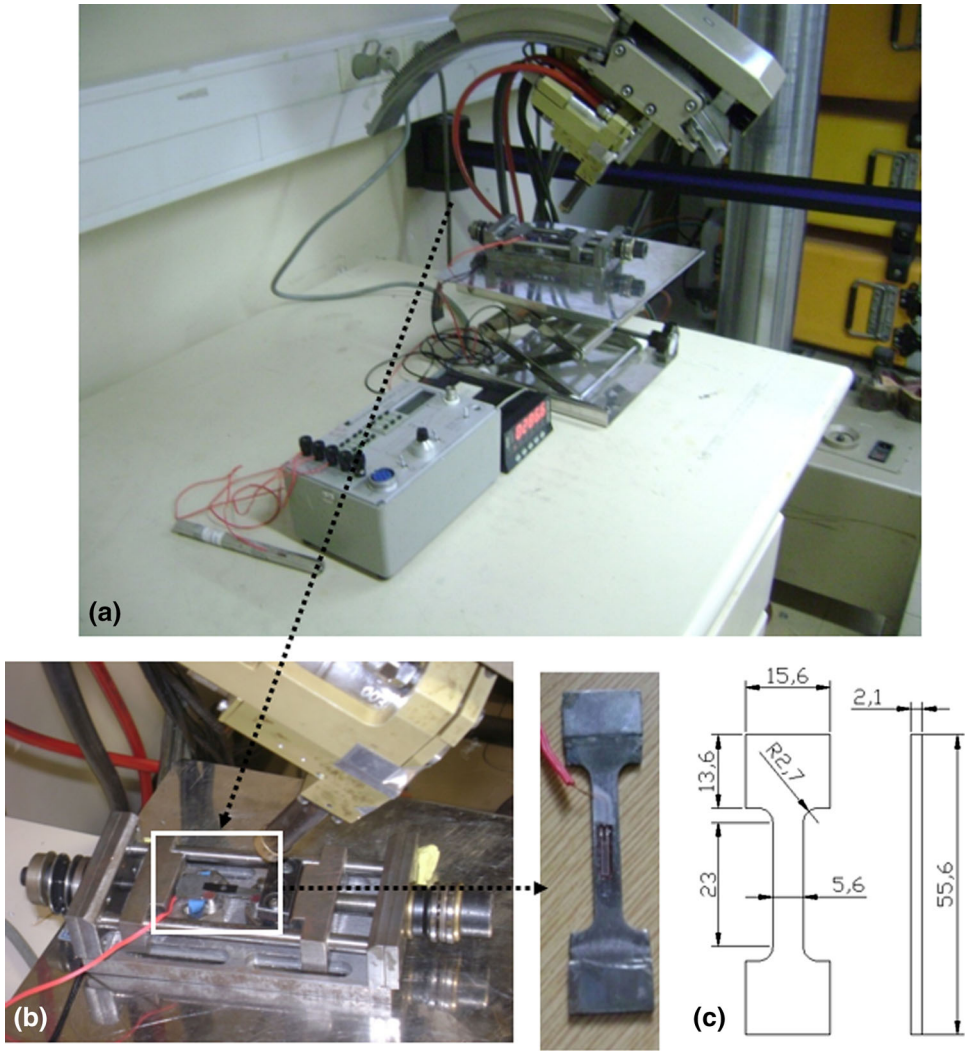

Fig. 3 Experimental setup for XRD measurement used for the "in-situ" tensile test. (a) XRD apparatus, (b) tensile test machine, (c) specimen geometry

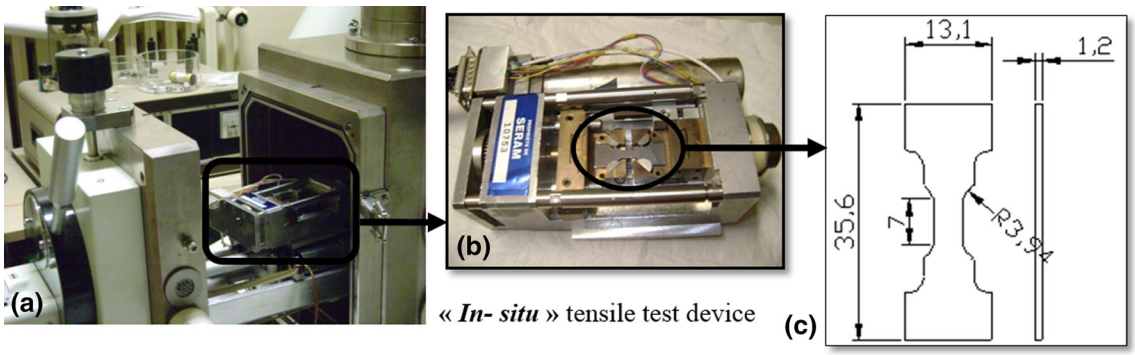

Fig. 4 Experimental setup used for the "in-situ" tensile test under scanning electron microscope. (a) SEM chamber, (b) tensile test machine, (c) specimen geometry

– The ferrite exhibits almost a perfect plastic flow for a large strain range with low work hardening.
– The ferrite flow stress increases gradually from 6% of total strain for the coarse pearlitic structure and from 8% of total strain for fine pearlitic structure. This change of plastic behavior is related to the evolution of stress partitioning between ferrite and cementite under the imposed total strain. Therefore, an increase in the ferrite stress level, at this stage of plastic deformation, was clearly observed. This increment was attributed to the load transfer from cementite to ferrite as a consequence of beginning of cementite fracture.

4.2 Effect of Interlamellar Spacing on Plastic Deformation Mechanism and Damage Mode

The processes governing the deformation and the damage of the two annealed pearlitic structures and their consequences on the ferrite behavior were investigated on nanometer and micrometer length scales.

4.2.1 EBSD Analysis. The local crystal orientations were investigated using EBSD. The IPF map of the deformed samples provides a micrograph showing the local pearlite colony orientations with respect to the tensile loading "Y" axis, (Fig. 6a). The inset represents the applied color code for the referenced poles. It can be seen that, the C70 steel includes pearlite colonies which are randomly oriented with respect to tensile axis. On the basis of calculated Schmid factor, the processing image reveals a contrast which allows to distinguish between the more favorably oriented colonies to activate slip systems (bright grains) from the more resistant to plastic flow (dark grains), (Fig. 6b). Closer examination of the highly deformed colonies reveals that slip takes place in some clearly defined planes (arrows), throughout the whole pearlite colonies, (Fig. 6c and d). The stereographic projection insert shows the slip direction of these pearlite colonies. A higher magnified EBSD scan depicts an offset of cementite plate along the shear band as shown by the selected encircled area (Fig. 6d). Orientation of shear bands to the tensile axis is due to the operative ferrite slip $\{110\}_{\alpha}$ plane near the maximum shear stress plane oriented at 45° with respect to the tensile axis. For supporting this assumption, two EBSD pole figures were taken at the same analyzed zone, they showed that crystallites are aligned not far from the $\{001\}\langle 010\rangle$ texture component (Fig 6e and f). Based on the stereographic projection, it can be concluded that shear band is tilted almost to 45° from the tensile axis. Despite the high total strain of more than 15%, there is only one single slip system visible over the whole examined pearlite colonies. Therefore, EBSD examination indicates a heterogeneous deformation in the highly strained zone (near the fracture) at micrometer scale, which integrates a random distribution of pearlite colonies (within 60 × 50 μ). At sub-micrometer scale, GAM images provide information about the misorientation distribution inside the pearlite colonies and which results from plastic deformation (Fig. 7). A misorientation profile, along the highly deformed pearlite colonies (with the highest Schmid factor (0.5)), calculated with respect to the starting point of the profile as indicated in Fig. 7(b), shows an important increase in the misorientation ranging from 0.5 (accuracy threshold) to 15°, (Fig. 7b and d). The large gradient in misorientation is often attributed to the dislocation pile-ups. On the contrary, the slightly deformed pearlitic grains with low Schmid factor (near zero) show a slight increase in the misorientation from 0.5° to 4° (Fig. 7c and e). The small misorientation gradient is considered to be the consequence of homogeneous distribution of the dislocation sources. It should be noted that the misorientations inside pearlitic colonies increase with the increase in the local deformation characterized by high value of the Schmid factor. These misorientations are the result of the global deformation of the pearlite colonies. Therefore, EBSD analysis did relate the low misorientation for homogeneous deformation (slightly deformed colonies) to the large misorientation for heterogeneous deformation (highly deformed colonies).

The EBSD results have been verified for other regions integrating a large amount of perlitic colonies. These regions correspond to the microstructure resulting from the two annealing treatment.

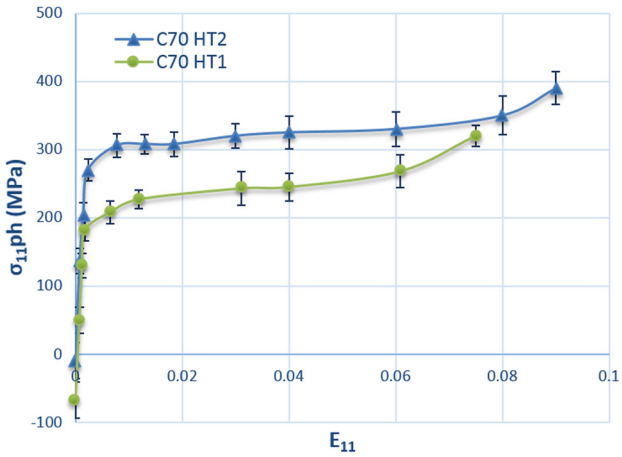

Fig. 5 Evolution of ferrite stress σ_{11} vs. total imposed strain E_{11} measured using x-ray diffraction during "in-situ" tensile tests for the two pearlitic microstructures

4.2.2 SEM "in-situ" Tensile Test Analysis. The SEM "in-situ" tensile test investigation indicates that the micromechanisms of deformation and damage are quite similar for both coarse and fine pearlitic structures.

- Deformation Mechanisms

The analysis of microstructure changes under the loading of numerous pearlite colonies reveals a gradual transition from a homogeneous deformation substructure to a heterogeneous one with an increase in the macroscopic-imposed strain:

- At low strain level (less than 5%), homogeneous deformation occurs during the first stages of straining by elasto-plastic elongation of colonies with lamellae parallel to the tensile axis. This elongation leads to an apparent thinning of continuous cementite lamellae resulting from the reduction of the interlamellar spacing. Lamellae inclined to the

Table 3 X-ray diffraction parameters

Radiation	*Cr Kα* λ = 0.22911 nm				
Voltage	20 kV				
Current	5 mA				
X-ray diffraction planes	{2 1 1}	2θ = 156°			
ϕ angles	0°				
ψ angles	39.23°	35.84°	32.3	28.56°	24.46°
	19.76°	13.83°	0.0°	−9.73°	−17.02°
	−22.21°	−26.57°	−30.47°	−34.10°	−37.55°

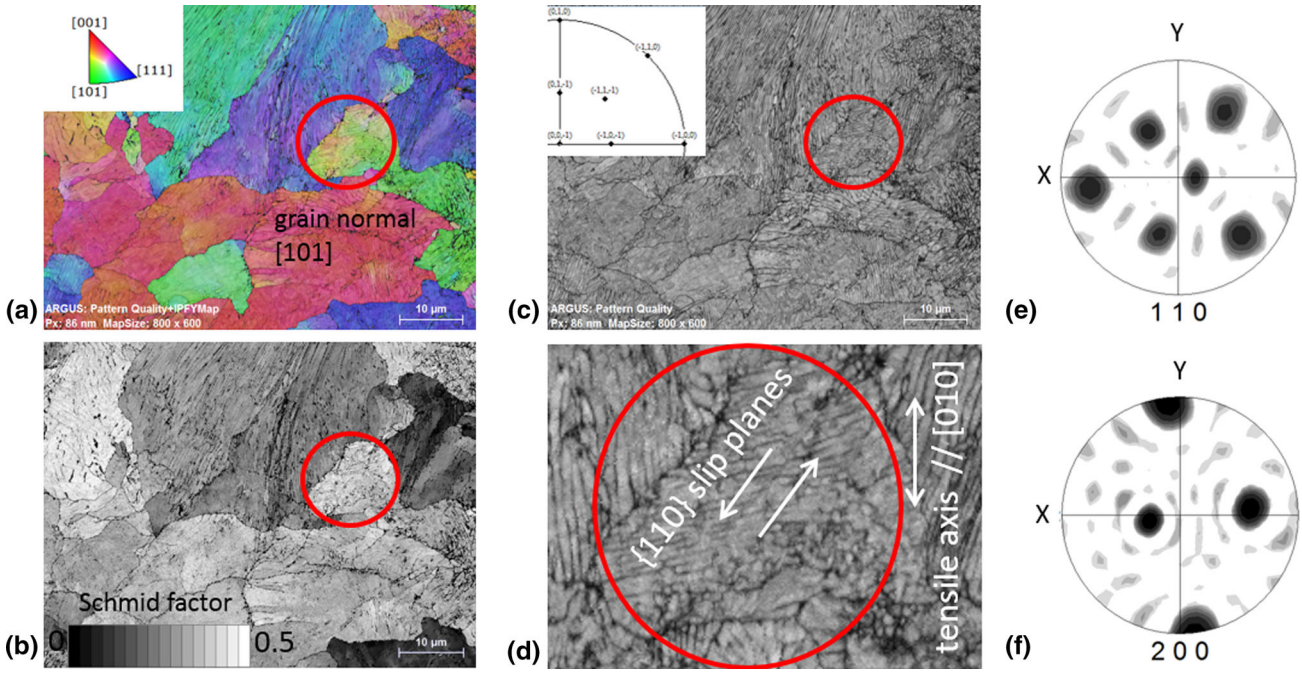

Fig. 6 Local crystal orientation of C70 (HT1), (a) IPF map of the deformed samples with respect to the tensile loading "Y" axis, (b) Schmid factor map, (c) pattern quality image, (d) zoom of the selected area, (e) pole figure (110) and (f) pole figure (200) from the selected area

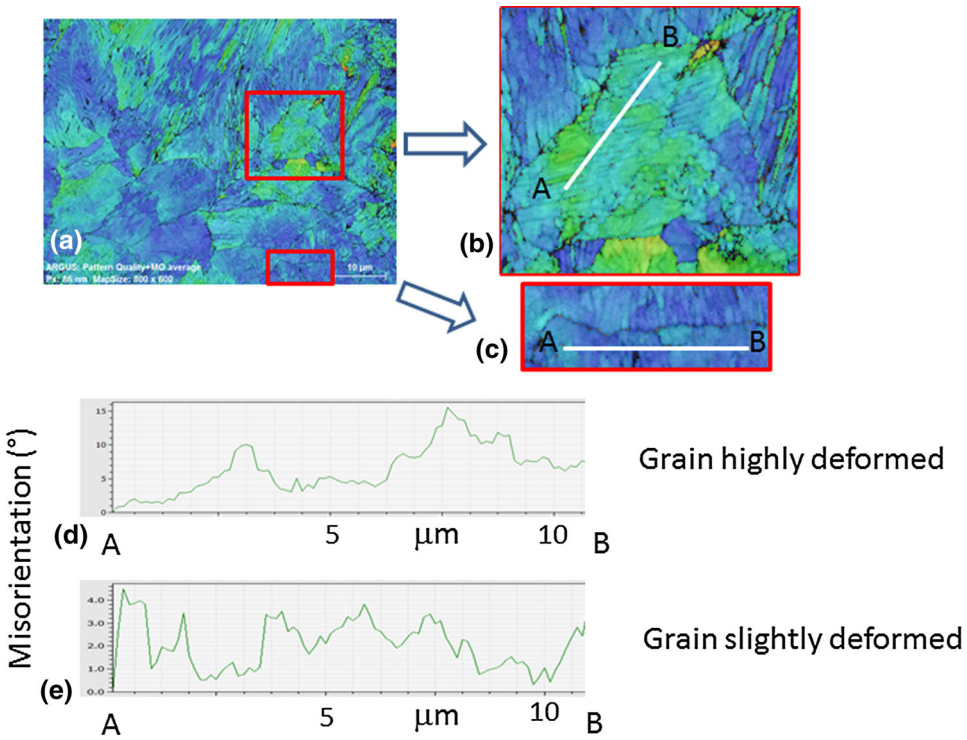

Fig. 7 (a) Grain average map from zone near fracture of C70 (HT1), (b) zoom from a high Schmid factor area, (c) zoom from a low Schmid factor area, (d) misorientation profile from zone (b), (e) misorientation profile from zone (c)

tensile axis tend to be rotated by the deformation of ferrite.

- At high strain level (more than 7%), deformation becomes gradually inhomogeneous by the activation of a single slip system in favorably oriented pearlite colonies. The slip results in the formation of steps which show straight slip bands on the surface of the polished tensile sample. Shear bands indicating large number of slip steps on closely spaced parallel slip planes are oriented at nearly 40 to 50° with respect to the tensile axis. They appear in pearlite co-

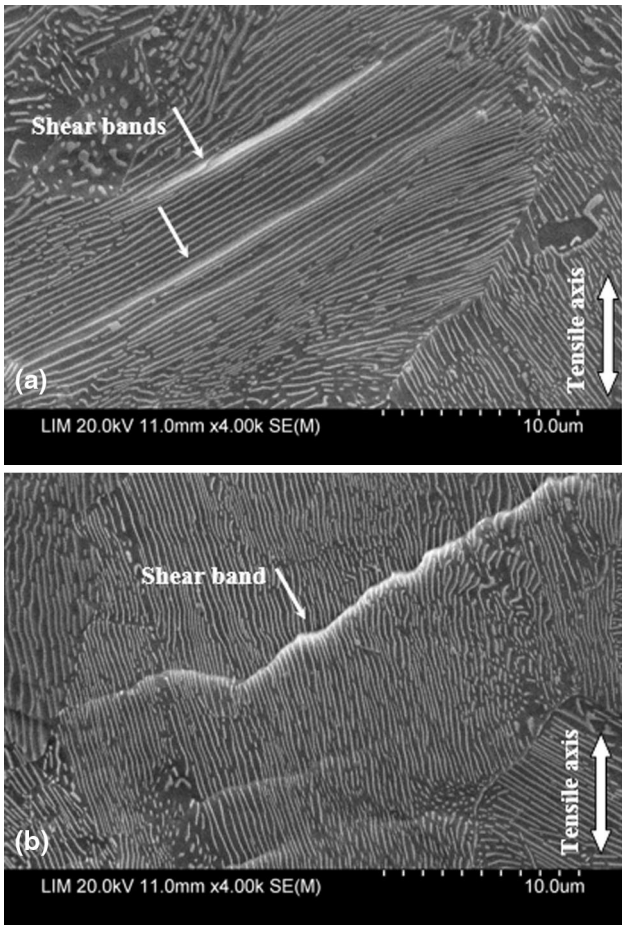

Fig. 8 Heterogeneous deformation generated by tensile loading of C70 (HT1) microstructure at strain level (E_{11} = 7%): (a) shear bands in pearlite colony with cementite lamellae inclined to the tensile axis; (b) shear bands in pearlite colony with cementite lamellae quite parallel to the tensile axis. (Micrographs were obtained from homogeneous strained parts)

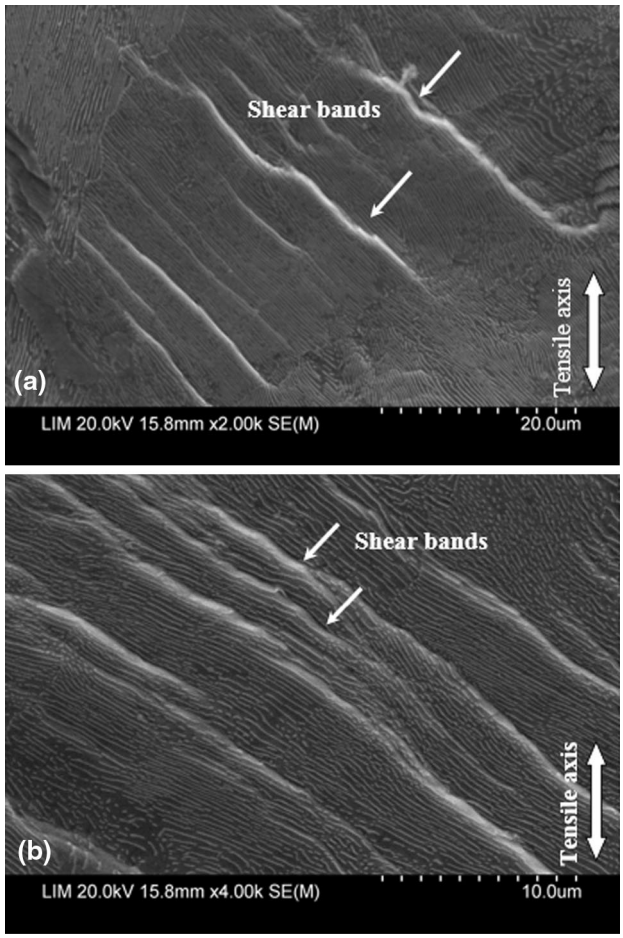

Fig. 9 Heterogeneous deformation generated by tensile loading: Narrow bands of locally intense shear: (a) total imposed strain E_{11} = 13%, (b) total imposed strain E_{11} = 15%. (Micrographs were obtained from homogeneous strained parts)

lonies with cementite lamellae parallel (Fig. 8b), and inclined to the tensile axis (Fig. 8a). At high strain, shear bands become more intense, indicating that large steps have been formed by localized deformation (Fig. 9). Shear bands propagate from favorably oriented colonies to undeformed ones by an easy shearing of boundaries (Fig. 8b). The deformation of cementite seems to be confined in the slip band regions by an offset of lamellae until fracture along the same slip bands (Fig. 10). For pearlite colonies with lamellae approximately transverse to tensile axis, bending and kinking phenomena appear at strain level of E_{11} = 6% which corresponds to a tensile stress ratio of 1.75 for coarse pearlite (Fig. 12a and b). These deformation modes can be attributed to compressive stresses resulting from imposed strain. It has also been shown that buckling of adjacent lamellae increases when increasing the loading stress level (Fig. 11c), and leads to local fracture of cementite plates (Fig. 11d).

These elementary mechanisms of plastic deformation operate similarly for the two annealed pearlitic microstructures. However, they occur in the earlier straining stages for coarse pearlitic structure and the shear bands seem to be narrower and less intense for fine pearlite than for the coarse one.

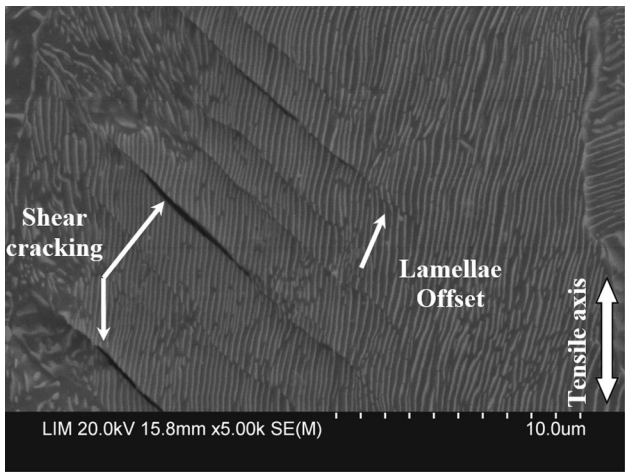

Fig. 10 Nucleation and growth of damage in loaded C70 (HT1) microstructure: offset and nucleation of cracks in shear bands (E_{11} = 15%). (Micrographs were obtained from zone near to fracture)

- Damage Mode

XRD "in-situ" tensile tests indicate that damage nucleation coincides with a marked change of the ferrite plastic flow

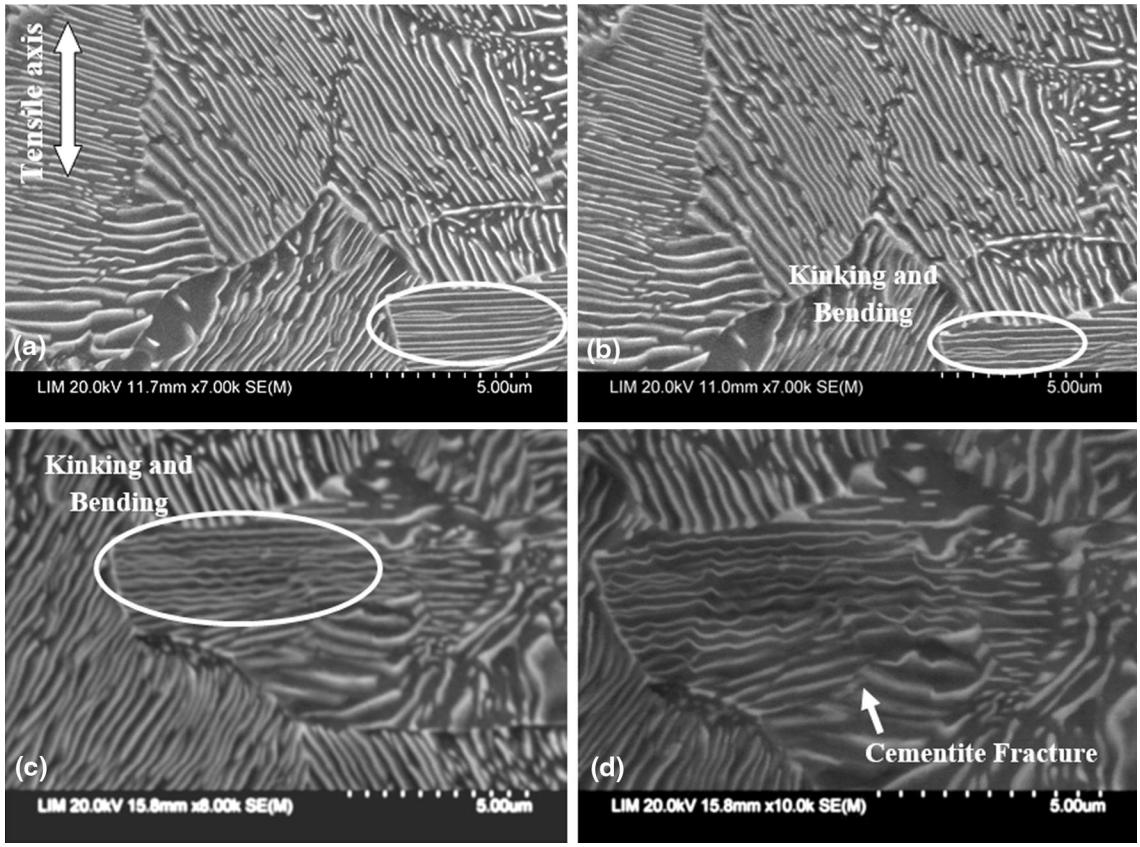

Fig. 11 Heterogeneous deformation generated by tensile loading of C70 (HT1) microstructure : (a) unloaded pearlitic colonies (E_{11} = 0 MPa); (b) beginning of kinking and bending of transverse pearlite colony at imposed strain: E_{11} = 6%; (c) buckling of adjacent lamellae at imposed strain E_{11} = 9%: (d) fracture of cementite lamellae at E_{11} = 12%. (Micrographs were obtained from homogeneous strained parts)

regime, as shown in Fig. 5. Indeed, ''in-situ'' SEM tensile tests reveal elongation and brittle fracture of cementite lamellae parallel to the tensile axis at an imposed macroscopic strain around 9% for pearlite structure with Sp = 170 nm and 6.5% for Sp = 230 nm. It can be seen that originally continuous cementite lamellae parallel to the tensile axis (before deformation) have broken into numerous fragments after straining at plastic strain level E_{11} = 6.5% (Fig. 12). Otherwise, cementite lamellae show neither obvious thinning nor necking. Their rupture seems to occur in a brittle manner.

For higher imposed strain (E_{11} = 11%), damage developed by shear micro-cracks along the slip bands and fracture of the cementite can be seen to occur along the slip bands (Fig. 13). In addition, crack growth is assisted by cementite fracture. Regions ahead of micro-cracks are subject to large biaxial tensile stress, which is responsible for activating a second slip system. The gradual localization of shear strain in the second slip system causes the nucleation of secondary micro-cracks (Fig. 14). The linking up of many micro-cracks leads to the development of crack networks (Fig. 15).

5. Discussion

It is established in this study that annealing treatment of C70 carbon steel controls the interlamellar spacing of fully pearlitic structure and accordingly the yielding limit as well as the occurrence of induced plastic damage. Annealing treatment HT2, giving low interlamellar spacing (Sp = 170 nm), confers to pearlite structure of C70 steel the highest yielding limit (σ_y = 498 MPa) compared with that of coarse pearlite (σ_y = 396 MPa and Sp = 230 nm).The ''in-situ'' x-ray tensile tests provide a ferrite yielding stress in the same ratio of pearlite yielding stress and the inverse of the interlamellar spacing (S_p) ratio :

$$\frac{\sigma_y Fe\alpha(HT2)}{\sigma_y Fe\alpha(HT1)} \approx \frac{\sigma_y pearlite(HT2)}{\sigma_y pearlite(HT1)} \approx \frac{S_p(HT1)}{S_p(HT2)} \approx 1.3$$

This result is supported by the EBSD and SEM analysis confirming that pearlite yielding is controlled by the onset of deformation in ferrite, which is likely controlled by dislocations-cementite plates interactions under loading. Therefore, cementite lamellae separated by Sp, are assumed to act as barriers for dislocation movements and leads to the dislocation pile-ups. This result corroborates Li et al. (Ref 15) analysis of AISI 1080 deformation substructure. They observed, by ''in-situ'' TEM tensile tests, the dislocations initiated at cementite-ferrite interfaces, trapped between the lamellar layers and bow in the direction of the applied stress. They added that these dislocations move on their slip plane with the increase of applied stress and pile-up at the ferrite-cementite interface where they activate other dislocation sources in the adjacent lamellae. These observations are consistent with EBSD examinations, performed in this study that shows that low misorientations ($<5°$) are observed inside the less deformed pearlite colonies (Fig. 7e), and that ''in-situ'' SEM examinations confirmed the homogenous deformation of pearlitic structure during the first stages of plastic yielding. Therefore, at low strain level, deformation of pearlite microstructure is

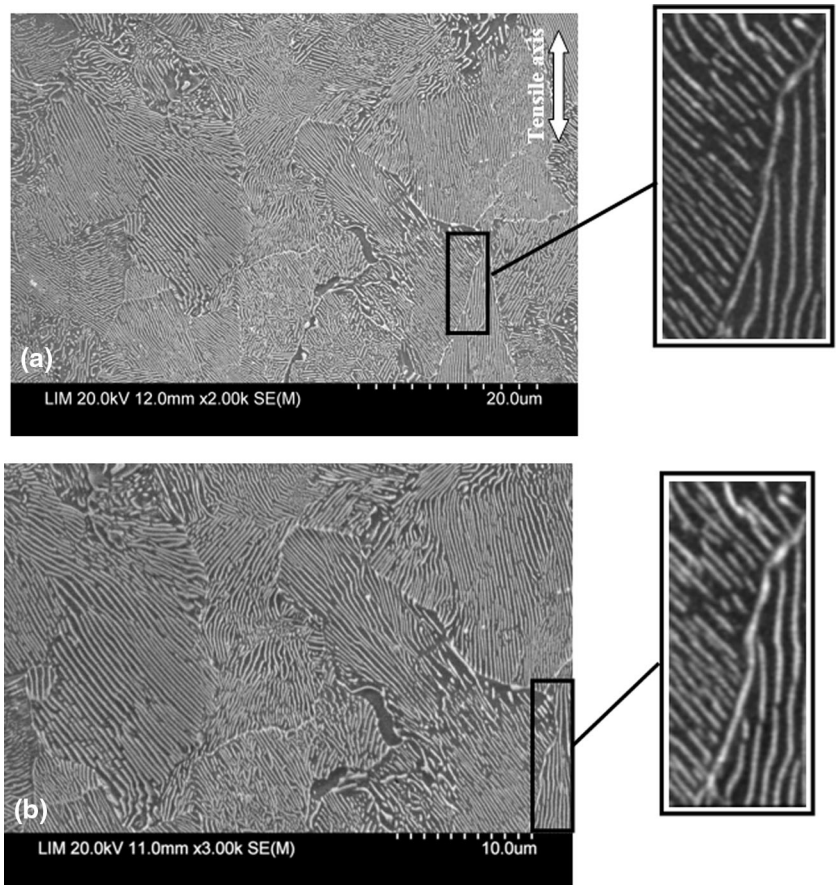

Fig. 12 Deformation and damage mechanisms of cementite phase in loaded C70 (HT1) microstructure: (a) unloaded pearlitic colonies (Σ_{11} = 0 MPa); (b) fracture of cementite lamellae at high stress level (E_{11} = 6.5%). (Micrographs were obtained from homogeneous strained parts)

likely ensured by homogeneous shearing through dislocation gliding which causes small misorientations of the pearlite colony. At high strain, a comparatively high misorientation, up to 15°, is produced (Fig. 7d) inside the most favorably oriented colonies, marked by the presence of localized shear bands (Fig. 6d). Moreover, the localized deformation in slip bands firstly appears in coarse pearlite after macroscopic strain level (E_{11} = 7%) and at higher value (E_{11} = 9%) in fine pearlite (Fig. 8). The EBSD KAM map showed a slip band distribution compatible with that of most favorably oriented pearlite colonies (high Schmid factor) with respect to the loading direction (Fig. 8). The orientation of shear bands to the tensile axis is due to the operative ferrite slip $\{110\}_{\alpha}$ plane near the maximum shear stress plane oriented at 45° with respect to the tensile axis. Their nucleation, preferentially in pearlite colonies with cementite lamellae parallel or slightly inclined to the tensile axis, is due to tensile stress acting either parallel or slightly inclined to the cementite lamellae, resulting from the highest stress incompatibility between cementite and ferrite. Dollar et al. (Ref 13) attributed the localized plastic flow at interfaces to this incompatibility, even at stresses lower than the yield stress. Dislocation pile-up leads to intense shear bands at higher strain. However, the bending-kinking observed in pearlite colonies with cementite plate dislocations gliding perpendicular to the tensile axis is assumed to be the result of the clustering of dislocations around the cementite lamellae. Previous work (Ref 14, 15) attributed the bending and kinking of cementite lamellae to the accumulation of dislocations around the 'free' end of cementite plates.

With increasing strain level, the number and the intensity of shear bands, across the randomly distributed colonies, increase and lead to more inhomogeneous plastic deformation of the two pearlitic microstructures (Fig. 9). However, the spacing between the slip lines appears relatively wide in the case of fine pearlite at equivalent imposed strain level. This result is consistent with that of Porter et al. (14) proving the tendency of coarse slip in the ferrite of coarse pearlite with interlamellar spacing of 400 nm. When shear becomes significant enough, an offset in cementite lamellae is observed and localized damage by shear cracking occurs. Crack growth is assisted by brittle fracture of cementite plates. The nucleation of shear cracking is observed mainly for coarse pearlite. This result is consistent with that of Porter et al. (Ref 14) on 0.8% carbon steel where it is reported that, in coarse pearlite, cracks are initiated at low strain level. However, in fine pearlite, crack initiation is a more difficult process requiring high plastic strains. Secondary slip is rather difficult to be active. The shear stress at the crack tip may be responsible for the activation of a secondary slip system, which is at the origin of nearby micro-crack initiation as observed in Fig. 14. Such micro-crack joins the main crack causing crack growth, which easily propagates along the original shear band under the combined action of shear and normal stresses produced by the impediment of slip in ferrite at the interface. These observations are conforming to those of Yongbo (Ref 16) on the 0.79% pearlitic steel.

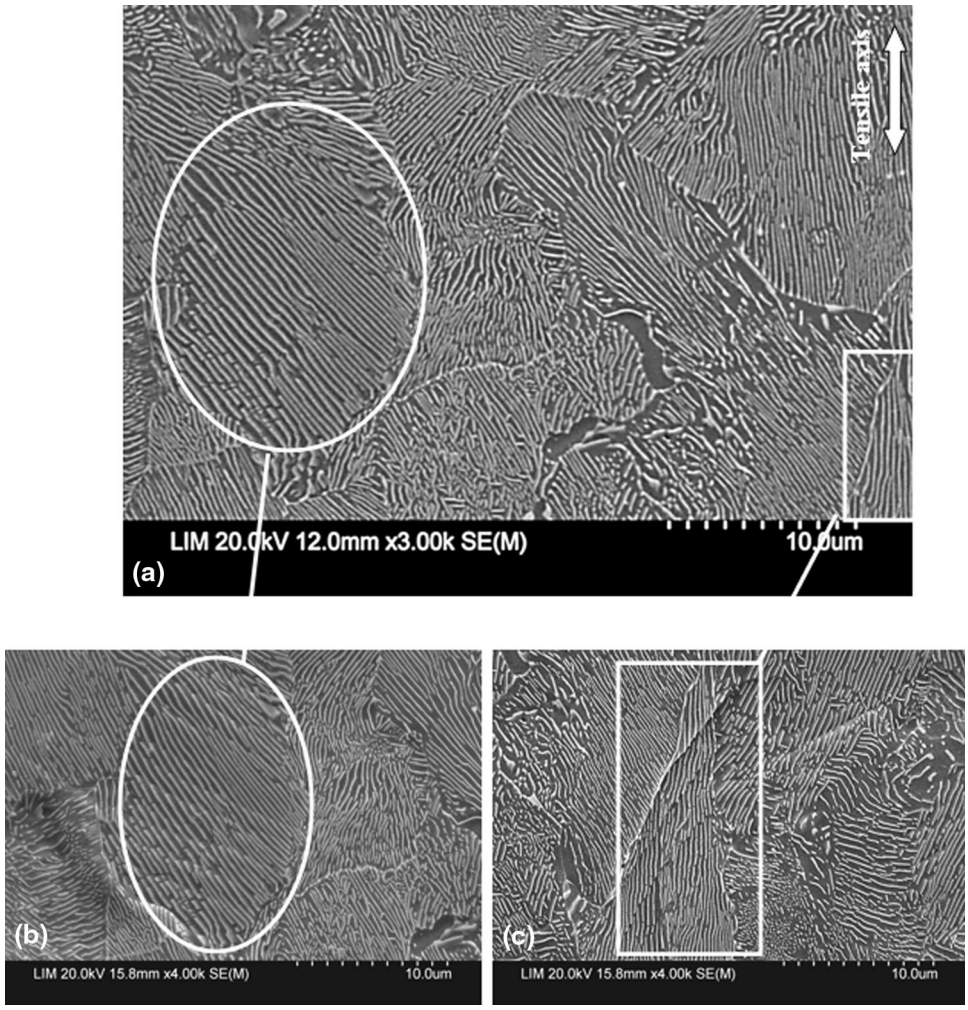

Fig. 13 Deformation and damage mechanisms of pearlite in loaded C70 (HT1) microstructure: (a) unloaded pearlitic colonies (E_{11} = 0 MPa); (b) shear bands (E_{11} = 11%), (c) shear cracking (E_{11} = 11%). (The same area as in Fig. 12)

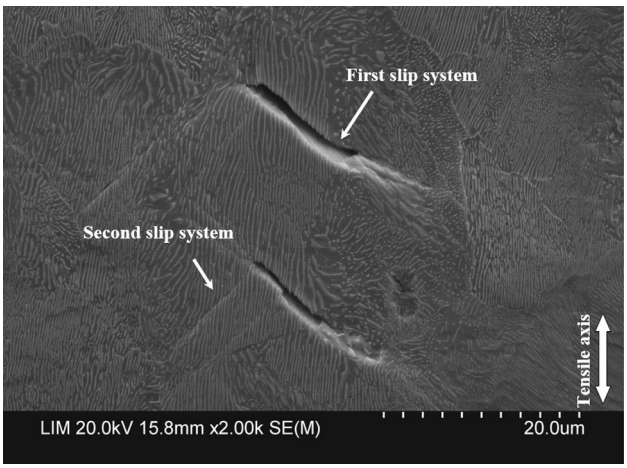

Fig. 14 Nucleation and growth of damage in loaded C70 (HT1) microstructure: (a) offset and nucleation of cracks in shear bands (E_{11} = 15%); (b) growth of cracks and activation of second slip system by increasing the applied stress level (E_{11} = 15%). (Micrographs were obtained from zone near to fracture)

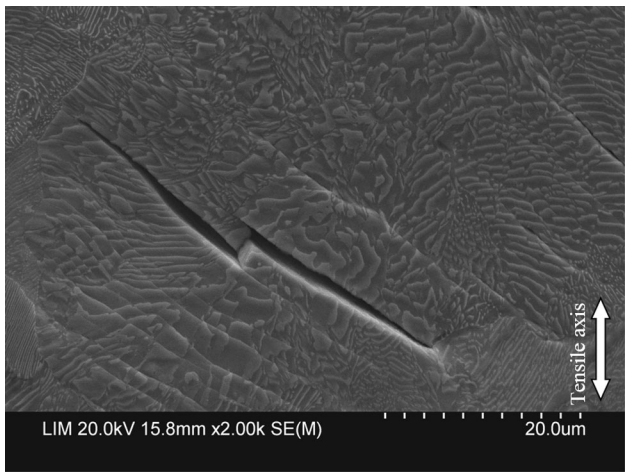

Fig. 15 Development of crack network (E_{11} = 15%). (Micrographs were obtained from zone near to fracture)

"In-situ" SEM examinations coupled with "in-situ" x-ray tensile tests attribute the greater resistance to the induced plastic damage of the fine pearlitic structure. Indeed, the cementite fracture was observed to occur firstly for coarse pearlite microstructure at plastic strain level equal to 6.5% comparatively to 9% for fine pearlite one. Thus, the increase of locally measured stress, as shown in Fig. 5, may be associated with the load transfer into the ferrite phase as a consequence of cementite lamellae fracture. This result is consistent with that of Joncour et al. (Ref 19) on duplex steel where it is indicated that the load is transferred into austenite once damage initiates in ferrite phase.

6. Conclusions

In this study, the mechanisms of deformation and damage of C70 pearlitic steel was investigated by combining EBSD, "in-situ" x-ray tensile tests, and "in-situ" SEM tensile test examinations. The main results can be summarized as follows:

- Pearlitic steel yielding is controlled by the deformation processes occurring in ferrite phase, which are influenced by the interlamellar spacing. The ferrite yielding limit of C70 pearlitic steel increases with the decrease in the interlamellar spacing : $\sigma_{y(Fe\alpha)} = 280$ MPa for Sp = 170 nm and $\sigma_{y(Fe\alpha)} = 210$ MPa for Sp = 230 nm. The ratio of pearlite yielding limits is in the same order of magnitude as the ratio of ferrite yielding limits and the inverse of interlamellar spacing ratio.
- The mechanisms of deformation and damage are quite similar for both coarse and fine pearlitic structures. At low plastic strains, pearlite tends to deform gradually with low misorientation, (less than 5°), this deformation is located inside the colonies and could be attributed to the dislocation source activity. At higher plastic strains, the deformation of pearlite is localized within the intense shear bands, across large pearlite colonies, with cementite lamellae parallel or slightly inclined to the tensile axis. The high misorientation up to 15° could be attributed to the dislocation pile-up. The nucleation of shear bands occurs at strain level equal to $E_{11} = 7\%$ for coarse pearlite and for fine pearlite at higher value of stain i.e., $E_{11} = 9\%$.
- The parallel cementite lamellae deform elastically until fracture occurs outside the shear bands. In pearlite colonies with lamellae perpendicular to the tensile axis, cementite kinks and bends. In the slip band region cementite deforms by an offset of lamellae.
- Fracture of cementite lamellae parallel to tensile axis marks the beginning of pearlite damage supporting the load transfer which is revealed by an increase in the stress level in the ferrite.
- Damage occurs by brittle fracture of elongated cementite lamellae parallel to the tensile axis and develops by shear micro-cracks along the slip bands. Crack growth is assisted by cementite fracture.
- The plastic-induced damage is delayed by the fine pearlite structure as the result of the local low shear stress ahead of the pile-up comparatively to the coarse pearlite. Indeed, the maximum pile-up stress is proportional to the number of dislocation in the pile-ups which are low in the fine pearlite.

Acknowledgments

G. Gonzalez would like to thank the financial support from CONACYT through Project No. 166896 necessary for EBSD detector acquisition. Part of this research was made during a sabbatical year of GG at PIMM. This visit was made possible by support from PASPA-UNAM, CONACYT and ENSAM-CNAM.

References

1. A.J. Perez-Unzueta and J.H. Beynon, Microstructure and Wear Resistance of Pearlitic Rail Steels, *Wear A*, 1993, **162-164**, p 173-182
2. G. Langford, Deformation of Pearlite, *Metall. Trans. A*, 1977, **8A**, p 861-875
3. O.P. Modi et al., Effect of Interlamellar Spacing on the Mechanical Properties of 0.65% C Steel, *Mater. Charact.*, 2001, **46**, p 347-352
4. O.P. Modia et al., Effect of Interlamellar Spacing on the Mechanical Properties of 0.65% C Steel, *Mater. Charact.*, 2001, **46**, p 347-352
5. A.M. Elwazri, P. Wanjara, and S. Yuea, The Effect of Microstructural Characteristics of Pearlite on the Mechanical Properties of Hypereutectoid Steel, *Mater. Sci. Eng A*, 2005, **404**, p 91-98
6. T. Shinozaki et al: Influence of Lamellar Spacing on Deformation Behavior of Pearlite Steels Studied by "in-situ" Neutron Diffraction. In: *The 3rd International Conference on Advanced Structural Steels Gyeongju*; *Korea*. 2006
7. C. Lei et al., Effect of Microstructure of Cementite on Interphase Stress State in Carbon Steel, *J. Iron. Steel Res. Int.*, 2007, **14**, p 31-38
8. O.P. Modi et al., Effect of Interlamellar Spacing on the Mechanical Properties of 0.65% C Steel, *Mater. Charact.*, 2001, **46**, p 347-352
9. C. Lei et al., Characterization of Deformability of Spheroidal Cementite by Residual Stress Measurement, *J. Mater. Eng. Perform.*, 2008, **17**, p 445-453
10. J.M. Hyzak and M. Bernstein, The Role of Microstructure on the Strength and Toughness of Fully Pearlitic Steels, *Metall. Trans. A*, 1976, **7A**, p 1218-1224
11. H. Yahyaoui et al., Effect of Interlamellar Spacing on the Elastoplastic Behavior of C70 Pearlitic Steel: Experimental Results and Self-consistent Modeling, *Mater. Des.*, 2014, **55**, p 888-897
12. A.R. Marder and B.L. Bramfitt, The Effect of Morphology on the Strength of Pearlite, *Metall. Trans. A*, 1976, **7A**, p 365-372
13. M. Dollar, I.M. Bernstein, and A.W. Thompson, Influence of Deformation Substructure on Flow and Fracture of Fully Pearlitic Steel, *Acta Metall.*, 1988, **36**, p 311-320
14. D.A. Porter, K.E. Easterling, and G.D.W. Smith, Dynamic Studies of the Tensile Deformation and Fracture of Pearlite, *Acta Metall.*, 1978, **26**, p 1405-1414
15. S. Li et al., In Situ TEM Studies of the Mechanisms of Crack Nucleation and Propagation in Fully Lamellar Microstructures, *Mater. Sci. Technol.*, 2003, **19**, p 902-906
16. X.U. Yongbo, Some Observation of Flow Localization and Shear Cracking in Pearlite During Deformation, *Chin. J. Met. Sci. Technol.*, 1989, **5**, p 135-137
17. X. Hu et al., Modeling Work Hardening of Pearlitic Steels by Phenomenological and Taylor-Type Micromechanical Models, *Acta Mater.*, 2006, **54**, p 1029-1040
18. I.C. Noyan and J.B. Cohen, *Residual Stress-Measurement by Diffraction and Interpretation*, Springer, Berlin, 1987
19. L. Le Joncour et al., Damage in Duplex Steels Studied at Mesoscopic and Macroscopic Scales, *Mech. Mater.*, 2010, **42**, p 1048-1063